

# Data-Driven Calibration of Large Liquid Detectors with Unsupervised Learning

Scott DeGraw\*, Steve Biller, Armin Reichold

*University of Oxford, The Denys Wilkinson Building, Keble Road, Oxford, OX1 3RH*

---

## Abstract

This paper demonstrates a novel method to extract photomultiplier tube (PMT) calibration timing constants in large liquid scintillation detectors from physics data using the machinery of unsupervised deep learning. The approach uses a simplified physical model of optical photon transport in the loss function, with PMT calibration constants treated as free parameters, and the simple assumption that individual events represent point-like emission. The problem is, thus, effectively reduced to that of regression on a very large scale, made tractable by deep learning architectures and automatic differentiation frameworks. Using data from the 9,300 PMTs in the SNO+ detector, the method has been shown to reliably extract 3 calibration constants for each of the over 7,500 online PMTs using radioactive background events. We believe that this basic approach can be straightforwardly generalised for a wide range of applications.

*Keywords:* Liquid scintillator, Neutrino detector, Calibration, Deep learning

---

## 1. Introduction

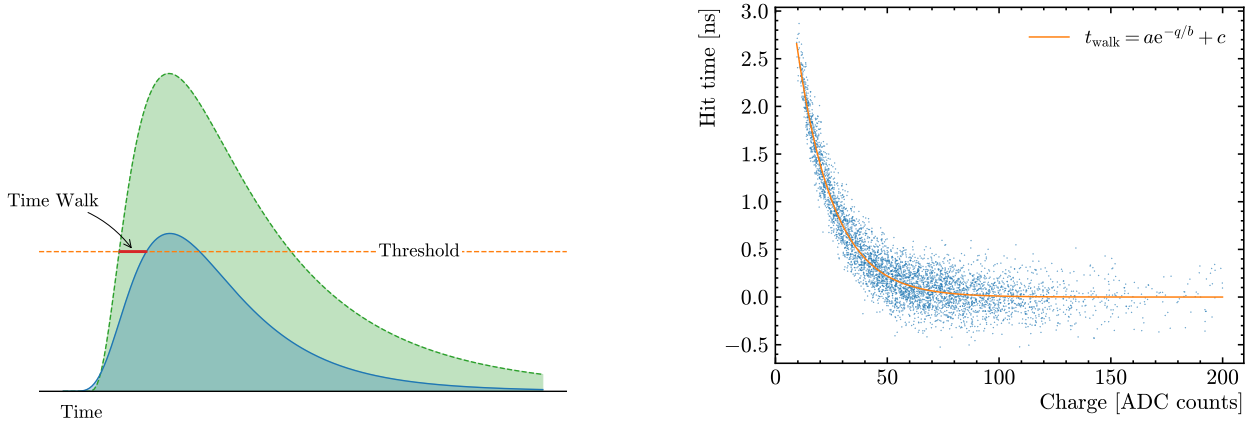
Large liquid scintillator detectors involve thousands of photomultiplier tubes (PMTs) to detect the scintillation light produced by charged particles depositing energy in the scintillating medium. The timing calibration of these PMTs (typically to the level of a few tenths of a nanosecond) is crucial to permit the accurate reconstruction of event positions based on the relative PMT hit times. For this, multiple effects need to be taken into account. Each PMT is connected to a data acquisition system via cables and front-end electronics that result in different time delays. In addition, PMT hit times are often only recorded when charge signals cross some pre-defined threshold above noise. This threshold gives rise to a charge-dependent *time walk* effect due to where the waveform is first sampled, which can vary in character for each electronic channel. An illustration of this effect is shown in Figure 1.

Standard methods for performing this type of calibration involve dedicated calibration light sources, either deployed *in situ* or fixed inside the detector. Deployed systems, such as

---

\*Corresponding author

*Email address:* scott.degraw@physics.ox.ac.uk (Scott DeGraw)



(a) An illustration of the time walk effect. The dashed line indicates a threshold applied to a typical PMT signal.

(b) A simulated demonstration of a time walk. Values are typical.

Figure 1: Time walk effect

laserballs (also known as diffuser balls) used in SNO [1], SNO+ [2], Super-Kamiokande [3] and JUNO [4] involve dedicated campaigns that are limited in how frequently they can be deployed, use light with different characteristics than physics events, generally stop physics data taking, and can carry a risk of contaminating the detector. Fixed systems in SNO+ [5], Borexino [6] and planned usage in Hyper-Kamiokande [7], typically use sources that are not in the detection volume and similarly produce light with wavelength spectra and timing that are different from those of physics events and, hence, can involve some extrapolation. An in situ method that uses data from actual events, without the requirement of specialised hardware, would therefore carry a number of advantages, provided that the calibration constants could be reliably extracted over a relatively short length of time.

The approach demonstrated here involves the use of data from known radioactive backgrounds in the SNO+ detector to perform a regression fit to 3 calibration parameters per PMT that describe individual time offsets and charge-dependent walk corrections, for a total of over 22,000 parameters. This is made easily tractable through the use of the robust gradient descent methods employed in automatic differentiation frameworks, which are well suited to this task.

## 2. Data-Driven Calibration

### 2.1. Detector

The target volume of SNO+ is a 12 m diameter acrylic vessel (AV) filled with 780 t of liquid scintillator. The AV is surrounded by an 18 m diameter PMT support structure holding approximately 9,300 inward facing PMTs, around 7,500 of which were online in the dataset used. The AV and support structure both reside 2 km underground in a cavity excavated in rock filled with 7 kt of ultra pure water. The AV is offset in the vertical direction to the centre of the PMT support structure by approximately 18.5 cm and has a neck for filling at the top. The PMTs are Hamamatsu R1408 PMTs inherited from SNO.

The liquid scintillator consists of Linear Alkyl Benzene (LAB) as a solvent and 2.2 g L<sup>-1</sup> of 2,5-diphenyloxazole (PPO) as a secondary fluor. The current phase of SNO+ as of December 2023 additionally contains a bisMSB wavelength shifter to improve light collection, but the dataset used here was taken before its addition. Comprehensive descriptions of the SNO, and SNO+ detectors can be found in [8, 9], respectively.

## 2.2. Timing Model

To sufficiently model the timing characteristics for PMT  $i$ , a decaying exponential as a function of PMT charge,  $q$ , was used to parametrize the time walk correction, in addition to a constant delay,  $c_i$ :

$$\tau_i(q) = a_i \exp(-q/b_i) + c_i. \quad (1)$$

The charge metric used is the PMT signal integrated over 70 ns measured in 12 bit analogue-to-digital counts. Adding an additional linear term with charge was tried but found to be unnecessary.

A priori, the time walk should be a monotonically decreasing function with charge  $q$ , meaning  $a_i \geq 0$  and  $b_i > 0$ . Numerical issues will also arise if  $b_i$  is non-positive, causing the exponent to diverge for large  $q$ . To constrain  $b_i$ , it is defined by a “softplus” transformation of unconstrained  $b_i^* \in \mathbb{R}$ :

$$b_i \equiv \frac{1}{\gamma_b} \log(1 + e^{\gamma_b b_i^*}), \quad (2)$$

where  $\gamma_b > 0$ . The value of  $\gamma_b$  is chosen to be large enough such that for typical values,  $b_i \approx b_i^*$ . The same constraint was found to be unnecessary for  $a_i$ .

For the starting seeds, a single typical example of timing parameters was found and then every PMT initialized with these values.

## 2.3. Time Residuals

PMT hit times,  $t_{\text{hit}}^i$ , are strongly and systematically dependent on the event vertex position. The hit times are also measured relative to the global trigger time, which occurs at an arbitrary offset from the actual event time,  $t_{\text{event}}$ . Assuming the event is point-like compared to the detector resolution, the remaining random element, primarily relating to the light emission time profile and PMT time jitter, is thus characterised by the time residual for each PMT hit  $i$ :

$$t_{\text{res}}^i = t_{\text{hit}}^i - t_{\text{event}} - t_{\text{TOF}}^i, \quad (3)$$

for PMT hit time  $t_{\text{hit}}^i$ , event time  $t_{\text{event}}$  and time of flight from vertex  $t_{\text{TOF}}^i$ .

For the correct position and event time, the time residual distribution across the hit PMTs should be sharply peaked, but with a long tail at late times due to scintillator reemission. Any errors in the PMT timing calibration or vertex reconstruction will then broaden this distribution. This forms the heart of this approach; individual events are assumed to produce

light emanating from a single position that varies from event to event, while calibration parameters remain constant over the entire collection of events. Individual event positions are reconstructed using candidate calibration parameters to subsequently calculate the time residuals. The event positions and calibration constants can be adjusted until the time residual distributions are sufficiently narrow at their peak. To do this, we make a fit to the time residual distributions with a simple model that has a sharp peak but with a long tail to account for the scintillator reemission. Using this model as a log likelihood loss function, the event positions and calibration parameters can be optimized simultaneously using gradient descent methods. Since any errors in the candidate calibration parameters may lead to biases in the position reconstruction, the simultaneous vertex and calibration optimization is crucial.

For this calibration, we use  $^{210}\text{Po}$  alpha decays with  $Q = 5.4 \text{ MeV}$  [10] which gives approximately 0.45 MeV of visible energy (*i.e.* the equivalent energy of an electron that would produce the same amount of light) due to nuclear quenching. This is an abundant background in the SNO+ detector due to radon contamination and can easily be tagged by an energy cut. The  $\alpha$  particles leave micron length energy depositions in the scintillator, providing a point-like light source for calibration.

The time residual distribution for  $^{210}\text{Po}$  decays from MC is shown in Figure 2. This distribution needs to be modelled so that it can be used as a loss function for gradient based optimization. The Jones and Faddy skew- $t$  distribution,  $f(x)$ , was chosen with scale and shift parameters  $\mu$  and  $\sigma$ , and parameters that adjust the skew,  $\alpha$  and  $\beta$  [11]:

$$f(x) = A \left( 1 + \frac{x}{(\alpha + \beta + x^2)^{1/2}} \right)^{\alpha+1/2} \times \left( 1 - \frac{x}{(\alpha + \beta + x^2)^{1/2}} \right)^{\beta+1/2}, \quad (4)$$

with normalizing constant and beta function  $B(\alpha, \beta)$

$$A = \frac{1}{2^{\alpha+\beta-1} B(\alpha, \beta) (\alpha + \beta)^{1/2}}, \quad (5)$$

and normalized time residual

$$x = \frac{t_{\text{res}} - \mu}{\sigma}. \quad (6)$$

This is an extension of the Student's  $t$ -distribution, giving heavy tails, and allowing for non zero skew. The log likelihood is also simple enough to be used as a loss function. A convenient feature of this distribution is that it has support on the entire real line, so no discontinuities arise during training if an anomalous time residual is calculated. The fit is shown in Figure 2 and describes the distribution well enough for our purpose.

In this study, we calculate the time of flight assuming a simplified straight line path

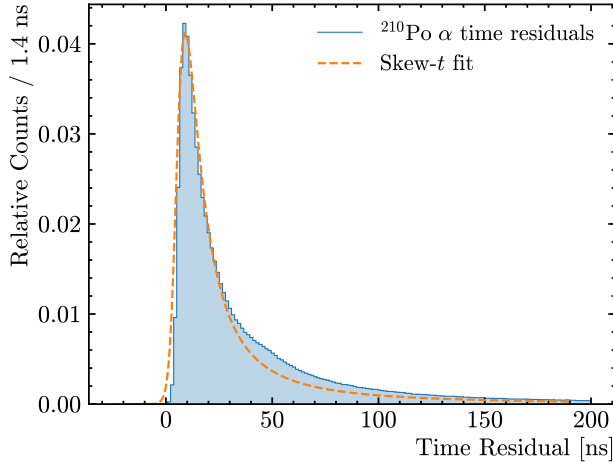


Figure 2: Time residual distribution for  $^{210}\text{Po}$  decays from MC. The Jones and Faddy skew- $t$  distribution is fit to the distribution and used as a loss function during training.

despite the high effective refractive index difference between scintillator and water (approximately 1.62 and 1.38, respectively). While future studies could try to implement more accurate methods, Monte Carlo (MC) simulation studies in Section 3.2 show that this simplification is adequate and more sophisticated methods are not expected to significantly improve the results. We use constant effective speeds of light in the scintillator and water of  $v_{\text{scint}} = 183.5 \text{ mm ns}^{-1}$  and  $v_{\text{water}} = 217.55 \text{ mm ns}^{-1}$ , respectively. These velocities were taken from earlier detector calibrations. The value of  $v_{\text{scint}}$  was also tuned to reduce the PMT  $z$  position dependence of the timing delays in Figure 3. Our calibration is not sensitive to small variations in these values. In principle, they could also be floated in the optimization, however we found these had weak convergence properties and did not seem to offer much advantage.

To achieve good timing resolution, a large dataset is needed to sufficiently sample the time residual distribution using hits from all the PMTs. This is provided by the abundant  $^{210}\text{Po}$  background in SNO+. In our case, datasets of around 7 million  $^{210}\text{Po}$  decays were used, collected over the space of 6 days.

Trying to simultaneously optimize the vertex position and time of each event along with the PMT timing calibration constants is a high dimensional problem and would be extremely challenging to perform directly. Instead of fitting the position and time of each event as individual parameters, a neural network is trained to reconstruct the event vertex from the PMT hit times. The neural network contains approximately 900,000 parameters which is much smaller than the  $4 \times 7$  million parameters for the position and time needed for a direct fit. To train, the position and time outputs of the neural network are used in conjunction with the candidate calibrated hit times to calculate the time residuals. The log likelihood given the skew- $t$  distribution (with parameters previously fit from MC) is then used to construct the loss function. The neural network and the timing parameters can then be optimized simultaneously through minimization of this loss function to yield the best timing model parameters. In this way, the reconstruction neural network does not need to

be trained on explicit MC truth labels, as is typical, and the calibration directly trains it on data in a form of unsupervised learning. This allows for a simple calibration procedure that can be performed end-to-end and requires minimal dependence on MC simulations.

#### 2.4. Model Architecture

The core of the deep learning model is a transformer encoder [12] based on earlier work on position reconstruction in SNO+ [13]. Transformers are powerful neural networks that use self-attention to learn relationships between different inputs. They are a natural choice for a scintillation detector with events that produce a variable number of PMT hits. The easily accessible, highly optimized implementation of transformers also makes this a computationally efficient architecture to train.

Each PMT hit forms an individual token, so the self-attention mechanism acts between every pair of hits. The input features to each token are the PMT ID and the hit time. Due to the presence of an arbitrary global time offset in the hit times, only relative hit times should be used by the model. To enforce this, the hit times are centred by the mean hit time of the event, ensuring that the model is invariant to any global shift. While the original transformer was applied to sequences of tokens by encoding the sequence position of each token, it is not obvious how meaningful sequences could be constructed from PMT hits. The hits could be ordered by hit time, but PMT hit times are not evenly spaced, so this would not fully capture the timing information. Therefore, no sequence position encoding is used to maintain hit permutation invariance.

To construct each token, each PMT is given an ID (from Equation 8) and each ID is given an embedding of dimension 64 that is learned during training. The hit time is passed through a multilayer perceptron with a tanh activation and a single 512 dimension hidden layer to give a matching length 64 embedding. The final token is then formed by summing these two embeddings together.

The transformer block has 6 layers, each with 4 attention heads and a feed-forward hidden dimension of 128. To extract a global representation of the event, the output of the transformer is passed through a mean pooling layer to give a single vector of length 64 for the entire event. A linear layer is then applied to give the 4 outputs of the model: the  $x$ ,  $y$  and  $z$  position and the time  $t$  of the event.

#### 2.5. Calibration Procedure

The calibration procedure is as follows:

1. Batches of  $^{210}\text{Po}$  events are retrieved with the PMT hit charges  $q_i$  and uncalibrated times  $t_{\text{uncal}}^i$ .
2. These times are corrected according to the candidate PMT timing models:  $t_{\text{cal}}^i \equiv t_{\text{uncal}}^i - \tau_i(q_i)$ .
3. The  $t_{\text{cal}}^i$  and PMT IDs are passed to the transformer model to reconstruct the event position and time.
4. Using a straight line time of flight calculation the time residuals,  $t_{\text{res}}^i = t_{\text{cal}}^i - t_{\text{event}} - t_{\text{TOF}}^i$ , are calculated.

5. The loss is calculated as the negative log likelihood of the time residuals given the Jones and Faddy skew- $t$  distribution fit to the MC time residual distribution in Figure 2.
6. Using the loss, gradients are calculated on the PMT timing model and the transformer model parameters. Since  $t_{\text{cal}}^i$  is used as input into the transformer model and directly used in the time residual calculation, gradients are allowed to flow to the timing model in two different paths.

The calibration is performed using a batch size of 2048 events, using the Adam optimizer [14] and a fixed 500,000 batches are used. The 1cycle learning rate scheduler [15] is used to vary the learning rate from an initial value of  $2 \times 10^{-5}$  to a maximum of  $1 \times 10^{-3}$  at the first 30% of steps and then decreases to  $5 \times 10^{-8}$  at the last step. The model used for the timing in Equation 1 is a simple exponential model, so it benefits greatly from a small learning rate at the end of the calibration to fine tune the timing which the 1cycle scheduler provides. To enhance this small learning rate, the model at the final step is used for all results. The loss on the validation test set is not used to pick the final model checkpoint.

The model is implemented in PyTorch with the default PyTorch transformer implementation. On a single NVIDIA H100 96 GB GPU the calibration takes approximately 24 hours to complete.

### 3. Validation

#### 3.1. Event Selection

Events near the AV will have a larger number of paths that have large incident angles at the scintillator-water interface. This will mean the angle of refraction will be large and even may undergo total internal reflection which are both not modelled well by the straight line time of flight calculations. Therefore, a fiducial cut is made to remove events near the AV with a reconstructed radius (with respect to the centre of the PMTs) greater than 4 m. Additionally,  $^{210}\text{Po}$  rates are higher near the top of the detector on the AV edge, so the cut makes the event distribution more uniform. Since this cut relies on a position reconstruction that is itself reliant on a previous PMT timing calibration, this might raise a concern of a possible bias being introduced. However, MC studies, in which initial systematic reconstruction biases in the fiducial volume selection as large as 20 cm were introduced, indicate that the potential impact on derived time calibration constants is minimal, resulting in a final reconstruction bias of  $< 8$  mm. In standard calibrations we expect a bias of around 10 cm in magnitude. If desired, even this could be eliminated with iteration.

The data and simulations used in this analysis use runs immediately after completion of the SNO+ liquid scintillator fill in May 2022. This run range was chosen due to the high rate of  $^{214}\text{BiPo}$  coincidences from the elevated radon contamination from the fill operation. These can provide a useful dataset for comparing timing calibrations as performed in Section 3.3.2. MC studies were based on generated  $^{210}\text{Po}$  decays in the detector. For data studies, events were selected with reconstructed energies between 0.35 MeV and 0.55 MeV to select  $^{210}\text{Po}$  decays. Since the salient features of  $^{210}\text{Po}$  decays are point-like energy depositions, contamination with other events that are also relatively point like should not significantly affect the calibration. Both data and MC datasets use approximately 7 million events after cuts.

### 3.2. Monte Carlo Validation

Using MC allows us to explicitly validate the timing accuracy of the calibration method, since we can inject known timing models to “uncalibrate” the data and see how well our calibration recovers them. The timing models used are the same as those found after calibrating on data in Section 3.3. The uncalibration for each PMT is performed by taking the truth timing model for the PMT, finding the timing model value at the hit charge, and then subtracting the MC truth hit time with this timing model value. The calibration process is performed on this uncalibrated MC sample and the fitted timing models can be compared to the ground truth timing models that were used to uncalibrate.

The residual of interest to evaluate the accuracy of the timing model for PMT  $i$  is given by

$$\tau_i^{\text{fit}}(q_i) - \tau_i^{\text{truth}}(q_i), \quad (7)$$

for charge  $q_i$  where  $\tau_i^{\text{truth}}$  is the MC truth timing model and  $\tau_i^{\text{fit}}$  is the fitted timing model from the calibration method. Each PMT will have a different distribution of charges. Thus, in order to get a distribution of Equation 7 over all PMTs, 10,000 samples of  $q_i$  for each PMT are drawn from the corresponding PMT’s charge histogram, from which the above residual is calculated and binned. Since reconstruction is invariant to a global PMT time offset, the distribution is centred by the median of the distribution. The results are shown in Figure 3.

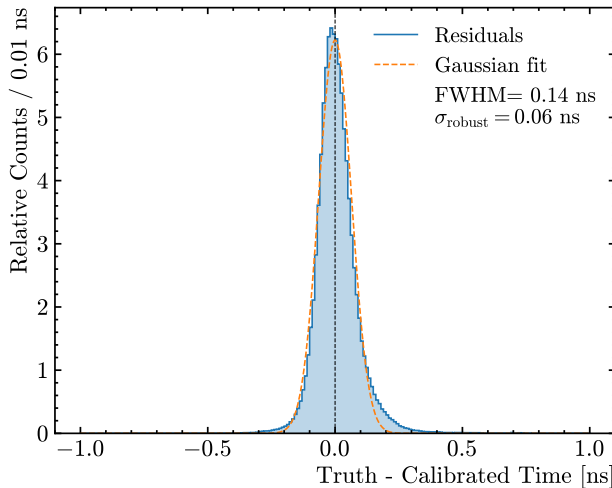


Figure 3: Distributions of PMT timing model residuals over all PMTs. The standard deviation of the residuals is estimated by taking the interquartile range and dividing by 1.35 for a robust estimate.

With a full width half maximum (FWHM) of 0.14 ns, this is much smaller than the transit time spread of 1.5 ns (RMS) for the Hamamatsu R1408 PMTs used in SNO+. The distribution of the residuals is skewed positively, which is likely due to the difficulty of fitting the timing model at the steep, low charge part of the spectrum, as shown in Figure 4.

An important consideration is whether the timing calibration has any dependence on the spatial position of the PMTs. The delays for each PMT are calculated by grouping

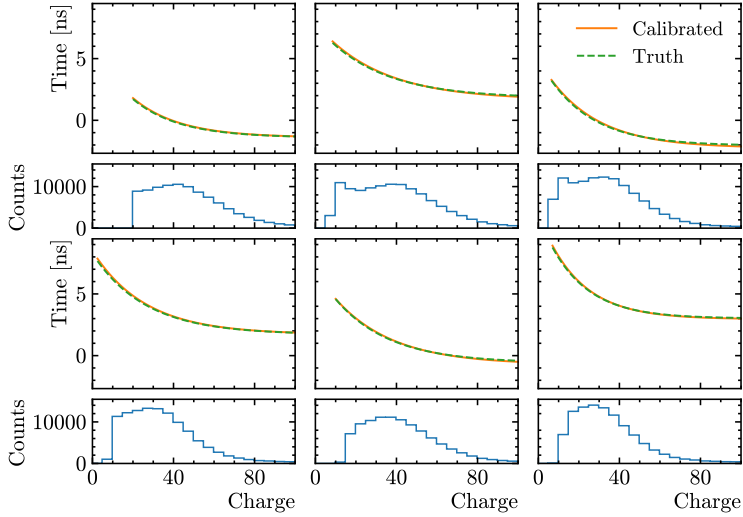


Figure 4: Examples of PMT timing models from MC truth and as fitted by the calibration method. The inset histogram shows the distribution of charges for this PMT. Time walks are only shown for charge bins which have non-zero counts.

the timing model residuals in Equation 7 by PMT and taking the median. These relative delays are then plotted against the PMT azimuthal angle  $\phi$  and  $z$  position in Figure 5. The delays show no significant dependence on PMT  $\phi$  or  $z$ . The large uptick at large  $z$  is due to the neck of the AV increasing the light path length. This optical effect of the neck is not easily modelled (and is not modelled in the standard calibration) so this feature is expected. Between  $-1.5$  m and  $1.5$  m, there is also a small increase in delay (where there are large  $z$  gaps between the PMTs), which is due to acrylic support plates attached to the AV that increase the path length.

The calibration results also remain reproducible across different random seeds, new MC simulations and small changes to optical parameters.

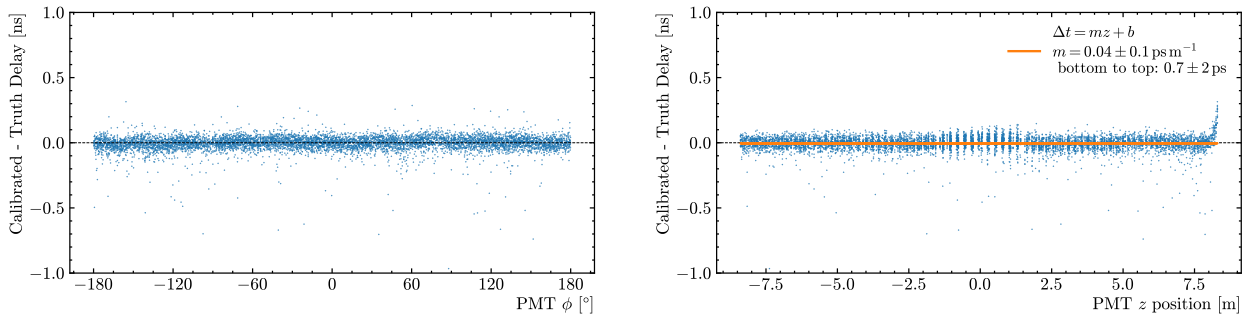


Figure 5: Each blue dot represents the delay residual for a PMT. For the PMT  $z$  position plot, a linear fit is shown in orange to illustrate the small dependence on  $z$  position. The “bottom to top” shows the difference in delay residual from the bottom to the top of the detector based on the linear fit.

Using a MC dataset not seen during calibration, the position reconstruction neural network was fed hit times calibrated by the procedure described here. This tests the overall

performance of the calibration and position reconstruction together. Position residuals compared to MC truth positions are shown in Figure 6. Position reconstruction performs well during the calibration, with minor biases. Given the simplified time residual and optical model used in the calibration, the resolution is surprisingly close to that of the standard position reconstruction algorithms for such alpha particles ( $\sim 215$  mm).

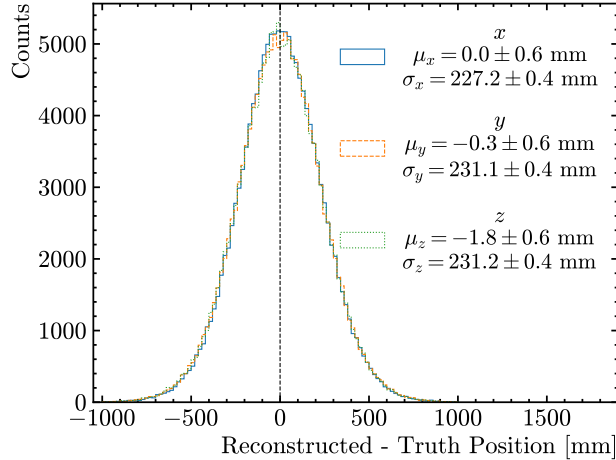


Figure 6: The position residuals (reconstructed - truth) as predicted by the position reconstruction neural network. The position reconstruction is carried out using PMT hit times determined by the calibration method described here.

### 3.3. Data Validation

Despite lacking ground truth timing models to compare to, some validation can still be made on real data. These include: 1) looking at the electronic channel structure of the delays found, 2) comparing to the standard SNO+ laserball calibration, and 3) looking at the position resolution using  $^{214}\text{BiPo}$  coincidences.

#### 3.3.1. Delays

The front end electronics for the PMTs are grouped together into 19 different crates. Each crate is subdivided into 32 cards that each have 16 PMT channels. A unique PMT ID is given to each PMT based on its crate, card and channel number:

$$\text{ID} = 512 \times \text{crate} + 32 \times \text{card} + \text{channel}. \quad (8)$$

Each PMT channel has a different electronic trace to traverse inside the crate and the cables should be the same length. Thus, the delays for PMTs across crates should generally be independent, but, within a crate, there should be a consistent pattern with PMT ID. This provides a characteristic structure that can be easily identified as a consistency check that the PMT calibration is performing as expected. The delays used here are given by the  $c_i$  from Equation 1.

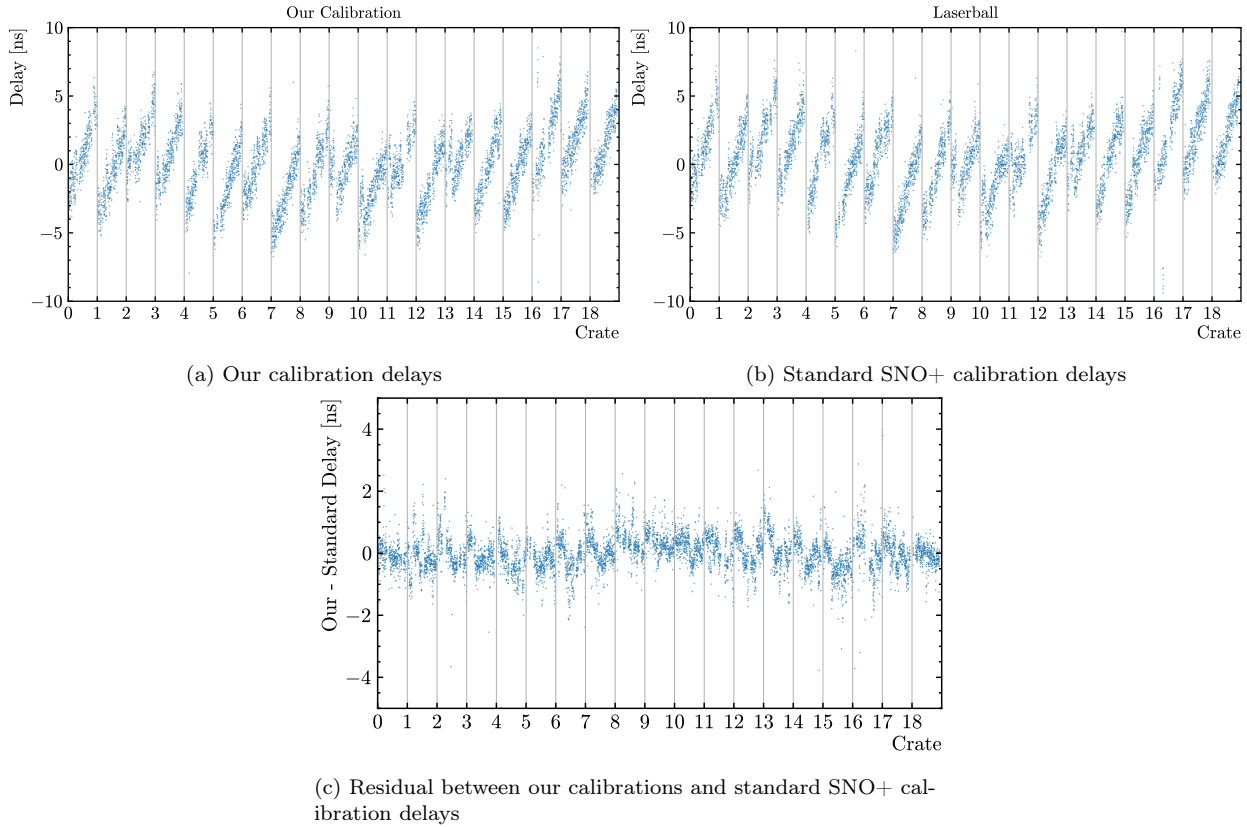


Figure 7: Comparison of delays found by our calibration method and the standard SNO+ calibration using the laserball.

The structure of our delays in Figure 7a show very similar crate by crate structure to the standard SNO+ delays Figure 7b [16]. The model has no knowledge of the crate/card/channel structure of the electronics (similarly to the laserball calibration) with the PMT IDs used purely as indices into lookup tables. Thus, the replication of this structure indicates that the calibration is finding physically meaningful results.

Comparing the delays from the two methods directly in Figure 8, there is a clear dependence of the delay residuals on the  $z$  position of the PMTs. This difference is approximately linear with a 1 ns difference from top to bottom of the detector based off the linear fit. However, this is consistent with the uncertainty in the absolute position of the laserball ( $\sim 10$  cm) that was used for the initial timing calibration [17].

### 3.3.2. $^{214}\text{BiPo}$ Coincidences

In addition to the  $^{210}\text{Po}$  decays used in our calibration, the intrinsic background from  $^{222}\text{Rn}$  in the SNO+ detector provides a useful source of  $^{214}\text{Bi}$ . The  $^{214}\text{Bi}$  decays to  $^{214}\text{Po}$  via a  $Q = 3.27$  MeV beta decay, shortly followed by an alpha decay with a  $164.3\ \mu\text{s}$  half-life in a sequence known as a  $^{214}\text{BiPo}$  coincidence [18]. The high  $Q$ -value of the  $^{214}\text{Bi}$  decay and short half-life of the  $^{214}\text{Po}$  decay allows these coincidences to be easily tagged. The position resolution of the detector is  $O(10\text{ cm})$ , which is much larger than the typical distance the

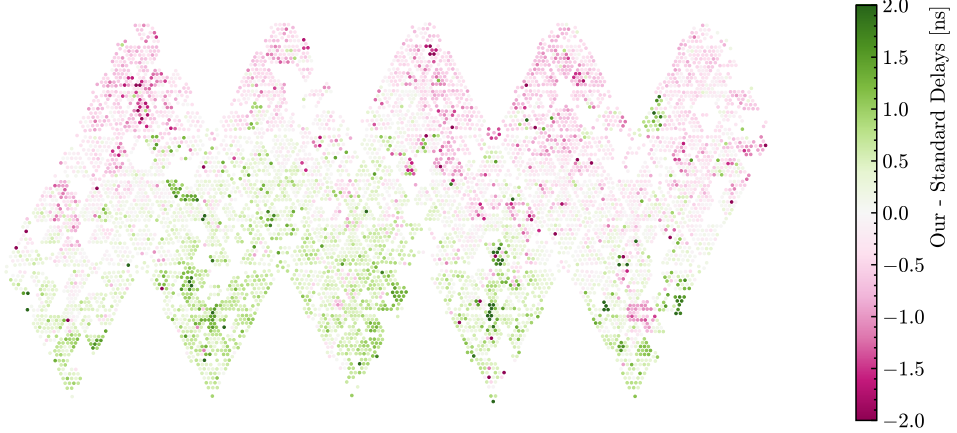


Figure 8: Residual between our calibrations and standard SNO+ calibration delays projected onto a flat map of the detector. The vertical  $z$  direction runs from top to bottom and azimuthal angle  $\phi$  runs horizontally.

$^{214}\text{Po}$  nucleus will travel before decaying due to the short half-life. However, it is still much longer than the 400 ns trigger window, so the individual  $^{214}\text{Bi}$  and  $^{214}\text{Po}$  decays will trigger separate events most of the time.

A purely data-driven metric of position resolution can thus be found by individually reconstructing the positions of the  $^{214}\text{Bi}$  and  $^{214}\text{Po}$  decays and finding the distance between the two reconstructed positions, denoted as  $\Delta R \equiv \|\vec{x}_{\text{Bi}} - \vec{x}_{\text{Po}}\|$ . Better timing calibrations results in better position reconstruction and, therefore, in smaller values of  $\Delta R$ .

Assuming the position reconstruction errors of the Bi and Po decays are each isotropic Gaussians with different widths, the distribution of  $\vec{x}_{\text{Bi}} - \vec{x}_{\text{Po}}$  should follow an isotropic 3-D Gaussian centred at zero with width,  $\sigma_{\Delta R}$ , given by the quadrature sum of the Bi and Po error widths. Thus,  $\Delta R$  will follow a chi distribution with three degrees of freedom otherwise known as a Maxwell-Boltzmann distribution which we can use to estimate  $\sigma_{\Delta R}$ . Due to accidentals contaminating the sample, we model the  $\Delta R$  distribution as a mixed distribution of the Maxwell-Boltzmann plus a flat background. This improves the quality of the fit compared to a pure Maxwell-Boltzmann. The distribution resulting from the data-driven method of this paper is compared with that from the standard SNO+ calibration in Figure 9. For this study, the same standard SNO+ likelihood-based position reconstruction is used for both, with results differing only as a consequence of which calibration time constants are used.

Our calibrations provide a statistically significant improvement in resolution. The fitted position resolution quadrature sum improves by  $\sim 6$  mm from  $200.2 \pm 0.5$  mm to  $193.9 \pm 0.4$  mm.

### 3.3.3. Detector Monitoring

Due to the ease of performing this calibration, it can be used to frequently monitor the stability of PMT timing calibrations. The first attempt at performing this calibration on the same dataset in Figure 7 showed significant deviations in the delays (defined by the  $c_i$  in Equation 1) for crate 11, as shown in Figure 10. This behaviour was entirely unexpected,

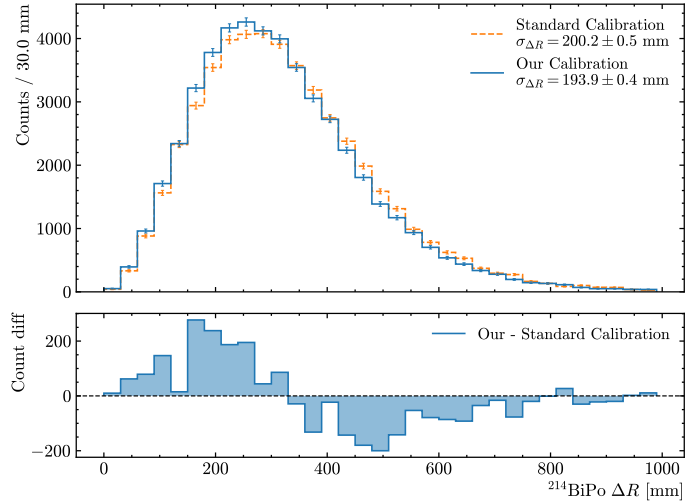


Figure 9: Distributions of  $\Delta R$  for  $^{214}\text{BiPo}$  coincidences in data. Distributions are shown for standard SNO+ calibration and our calibration. Combined Bi and Po position resolution values are shown.

but our calibration method is blind to crate segmentation and, once we were alerted to this, the effect could clearly be seen in the raw time residuals. Following a lower level electronics calibration, performed shortly after this dataset was taken, a repeated application of our calibration indicated that this deviation had disappeared. While the exact cause of this is still under investigation, the shift was clearly real and our calibration allowed us to identify when the issue occurred between normal calibration runs. This also highlights the utility of this approach as a continuous monitor of detector performance and an aid to diagnosing and correcting potential issues.

Except for Figure 10, all other results use data that have been reprocessed with this updated lower level calibration.

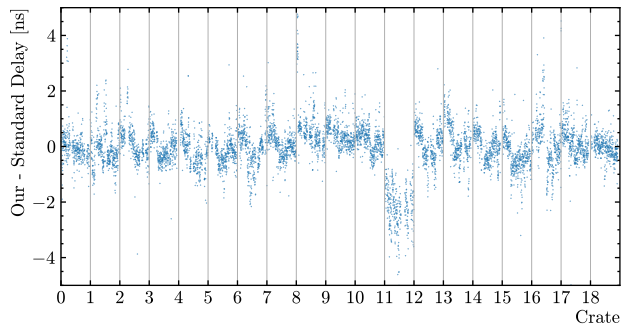


Figure 10: Delay residuals between our calibration and the standard SNO+ calibration for dataset taken before a lower level electronics calibration was performed.

## 4. Summary

A novel method of performing a PMT timing calibration in large scintillator detectors has been demonstrated through the application of unsupervised learning to the analysis of naturally occurring radioactive backgrounds. The approach leverages the machinery of deep unsupervised learning to simultaneously and reliably fit over 22,000 calibration parameters in the SNO+ detector, permitting a time calibration accuracy of 0.14 ns FWHM, based on MC simulation tests. Application to physics data from the SNO+ detector was found to reproduce the expected electronic structure of the PMT timing constants. Using an established SNO+  $^{214}\text{Bi}$  -  $^{214}\text{Po}$  coincidence event analysis as a benchmark, the calibration was shown to provide a statistically significant improvement in position resolution compared to the standard SNO+ laserball-based calibration. It was further able to correctly diagnose changes in calibration parameters that had previously been overlooked. This method has thus been shown to provide an accurate and reliable method to perform PMT timing calibrations using only physics data, without the resource intensive process of a dedicated hardware-based calibration.

The basic approach demonstrated here should not only prove useful for other large scale liquid detectors, but ought to be easily extendable for a wider range of other applications.

## Acknowledgments

This work was supported by the Science Technology and Facilities Council of the United Kingdom. The authors would like to thank the SNO+ collaboration for use of their data, RAT simulation and many useful discussions.

Appropriate representations of the data relevant to the conclusions have been provided within this paper.

## References

- [1] B. A. Moffat, R. J. Ford, F. A. Duncan, K. Graham, A. L. Hallin, C. A. W. Hearns, J. Maneira, P. Skensved, D. R. Grant, Optical calibration hardware for the Sudbury Neutrino Observatory, Nuclear Instruments and Methods in Physics Research Section A: Accelerators, Spectrometers, Detectors and Associated Equipment 554 (1-3) (2005) 255–265. [arXiv:nucl-ex/0507026](https://arxiv.org/abs/nucl-ex/0507026), doi:10.1016/j.nima.2005.08.029.
- [2] S. Valder, A. Gibson-Foster, E. Falk, S. Peeters, C. Mills, M. Nirkko, M. Rigan, J. Sinclair, A laserball calibration device for the SNO+ scintillator phase, Journal of Instrumentation 19 (01) (2024) T01005. doi:10.1088/1748-0221/19/01/T01005.
- [3] Super-Kamiokande Collaboration, Calibration of the Super-Kamiokande detector, Nuclear Instruments and Methods in Physics Research Section A: Accelerators, Spectrometers, Detectors and Associated Equipment 737 (2014) 253–272. doi:10.1016/j.nima.2013.11.081.

[4] Y. Zhang, J. Liu, M. Xiao, F. Zhang, T. Zhang, Laser calibration system in JUNO, *Journal of Instrumentation* 14 (01) (2019) P01009–P01009. [doi:10.1088/1748-0221/14/01/P01009](https://doi.org/10.1088/1748-0221/14/01/P01009).

[5] E. Falk, J. Lidgard, M. I. Stringer, E. Turner, Commissioning of ELLIE for SNO+, (2017). [doi:10.48550/ARXIV.1705.00354](https://doi.org/10.48550/ARXIV.1705.00354).

[6] B. Caccianiga, D. Franco, D. Giugni, P. Lombardi, S. Malvezzi, J. Maneira, G. Manusardi, L. Miramonti, G. Ranucci, O. Smirnov, A multiplexed optical-fiber system for the PMT calibration of the Borexino experiment, *Nuclear Instruments and Methods in Physics Research Section A: Accelerators, Spectrometers, Detectors and Associated Equipment* 496 (2-3) (2003) 353–361. [doi:10.1016/S0168-9002\(02\)01762-X](https://doi.org/10.1016/S0168-9002(02)01762-X).

[7] W. G. S. Vinning, The Narrow-beam Diffuser Subsystem of a Prototype Optical Calibration System for the Hyper-Kamiokande Detector (2019). [doi:10.48550/ARXIV.1904.01660](https://doi.org/10.48550/ARXIV.1904.01660).

[8] The SNO Collaboration, The Sudbury Neutrino Observatory, *Nuclear Instruments and Methods in Physics Research Section A: Accelerators, Spectrometers, Detectors and Associated Equipment* 449 (1) (2000) 172–207. [doi:10.1016/S0168-9002\(99\)01469-2](https://doi.org/10.1016/S0168-9002(99)01469-2).

[9] The SNO+ Collaboration, Current Status and Future Prospects of the SNO+ Experiment, *Advances in High Energy Physics* 2016 (2016) 1–21. [doi:10.1155/2016/6194250](https://doi.org/10.1155/2016/6194250).

[10] M. Shamsuzzoha Basunia, Nuclear Data Sheets for  $A = 210$ , *Nuclear Data Sheets* 121 (2014) 561–694. [doi:10.1016/j.nds.2014.09.004](https://doi.org/10.1016/j.nds.2014.09.004).

[11] M. C. Jones, M. J. Faddy, A Skew Extension of the  $T$ -Distribution, with Applications, *Journal of the Royal Statistical Society Series B: Statistical Methodology* 65 (1) (2003) 159–174. [doi:10.1111/1467-9868.00378](https://doi.org/10.1111/1467-9868.00378).

[12] A. Vaswani, N. Shazeer, N. Parmar, J. Uszkoreit, L. Jones, A. N. Gomez, Ł. Kaiser, I. Polosukhin, Attention is all you need, in: I. Guyon, U. V. Luxburg, S. Bengio, H. Wallach, R. Fergus, S. Vishwanathan, R. Garnett (Eds.), *Advances in Neural Information Processing Systems*, Vol. 30, Curran Associates, Inc., 2017.

[13] C. Hewitt, Machine learning for event reconstruction at SNO+, <https://indico.ipmu.jp/event/462/contributions/8724/> (Oct. 2025).

[14] D. P. Kingma, J. Ba, Adam: A Method for Stochastic Optimization (Jan. 2017). [arXiv:1412.6980](https://arxiv.org/abs/1412.6980), [doi:10.48550/arXiv.1412.6980](https://doi.org/10.48550/arXiv.1412.6980).

[15] L. N. Smith, N. Topin, Super-Convergence: Very Fast Training of Neural Networks Using Large Learning Rates (May 2018). [arXiv:1708.07120](https://arxiv.org/abs/1708.07120), [doi:10.48550/arXiv.1708.07120](https://doi.org/10.48550/arXiv.1708.07120).

- [16] F. Descamps, PCA calibration with SNO+ RAT, Internal SNO+ Document #1987 (May 2016).
- [17] J. R. N. Cameron, The Photomultiplier Tube Calibration of the Sudbury Neutrino Observatory, Ph.D. thesis.
- [18] S. Zhu, E. McCutchan, Nuclear Data Sheets for A=214, Nuclear Data Sheets 175 (2021) 1–149. doi:10.1016/j.nds.2021.06.001.